The Meteoritical Society

Meteoritics & Planetary Science 45, Nr 1, 55–72 (2010)
doi:10.1111/j.1945-5100.2009.01005.x

Iron oxides in comet 81P/Wild 2

John C. BRIDGES[1*], Mark J. BURCHELL[2], Hitesh C. CHANGELA[1], Nick J. FOSTER[2], J. Alan CREIGHTON[2], James D. CARPENTER[3], Steve J. GURMAN[4], Ian A. FRANCHI[5], and Henner BUSEMANN[5,6]

[1]Department of Physics and Astronomy, Space Research Centre, University of Leicester, Leicester LE1 7RH, UK
[2]Centre for Astrophysics and Planetary Science, School of Physical Sciences, University of Kent, Canterbury, Kent CT2 7NH, UK
[3]ESTEC, Keplerlaan 1, 2201 AZ Noordwijk, The Netherlands
[4]Department of Physics and Astronomy, University of Leicester, Leicester LE1 7RH, UK
[5]Planetary and Space Science Research Institute, Open University, Walton Hall, Milton Keynes MK7 6AA, UK
[6]School of Earth, Atmospheric and Earth Sciences, University of Manchester, Manchester M13 9PL, UK
*Corresponding author. E-mail: j.bridges@le.ac.uk

(Received 08 December 2008; revision accepted 21 September 2009)

Abstract–We have used synchrotron Fe-XANES, XRS, microRaman, and SEM-TEM analyses of Stardust track 41 slice and track 121 terminal area slices to identify Fe oxide (magnetite-hematite and amorphous oxide), Fe-Ti oxide, and V-rich chromite (Fe-Cr-V-Ti-Mn oxide) grains ranging in size from 200 nm to ~10 μm. They co-exist with relict FeNi metal. Both Fe-XANES and microRaman analyses suggest that the FeNi metal and magnetite (Fe_2O_3FeO) also contain some hematite (Fe_2O_3). The FeNi has been partially oxidized (probably during capture), but on the basis of our experimental work with a light-gas gun and microRaman analyses, we believe that some of the magnetite-hematite mixtures may have originated on Wild 2. The terminal samples from track 121 also contain traces of sulfide and Mg-rich silicate minerals. Our results show an unequilibrated mixture of reduced and oxidized Fe-bearing minerals in the Wild 2 samples in an analogous way to mineral assemblages seen in carbonaceous chondrites and interplanetary dust particles. The samples contain some evidence for terrestrial contamination, for example, occasional Zn-bearing grains and amorphous Fe oxide in track 121 for which evidence of a cometary origin is lacking.

INTRODUCTION

Since the recovery of the Stardust capsule in January 2006, samples from the coma of comet 81P/Wild 2 have started to reveal what this Jupiter-family comet is made of (Brownlee et al. 2006). Burchell et al. (2008) estimated that approximately 1200 particles larger than 1 μm had struck the cometary collector at 6.1 km s^{-1}. The high speed of the impact events causes some processing of the particles during capture. As discussed in Hörz et al. (2006) and Burchell et al. (2008), three types of tracks are found in the Stardust aerogel: Type A (relatively slender tracks that taper to an end where a "terminal" grain is found, which may, however, only be an unknown fraction of the originally incident particle), Type B (tracks with an initially bulbous cavity lined with fragments of the impactor and beneath which one or several slender tracks emerge, which again often contain terminal grains), and Type C (tracks with just a bulbous cavity lined with fragments of the initial particle). The incident particle may thus break apart during capture and also undergo heating as it passes through the aerogel. Hence, any cometary dust grain along an aerogel track should be considered as a fragment of the originally incident dust grain (which generated that aerogel track) and which may have undergone shock and/or heat processing during capture.

In the initial description following the preliminary examination phase, Zolensky et al. (2006) described the particles captured in the aerogel as an assemblage of ferromagnesian silicates (particularly forsterite and enstatite), Fe-Ni sulfides, and Fe-Ni metal, mainly in nanometer-size grains with relatively few larger, micron-size grains that are in terminal positions within impact

tracks. Similarly Hörz et al. (2006) and Kearsley et al. (2008) have shown that the Al foils that held the aerogel cells in place collected a similar assemblage consisting mainly of Mg-rich silicates and abundant Fe-Ni sulfides in micron-size crater residues. Flynn et al. (2006) and Flynn (2008) used synchrotron XRF to show that the composition of the cometary material in the aerogel tracks was similar to CI chondrites to within 35–60% for the major elements but with more variance for the moderately volatile elements which they showed were similar to anhydrous porous interplanetary dust particles (IDPs). The presence of refractory material and possibly chondrule fragments has been taken to indicate mixing between material formed in the inner Solar System and less refractory material that constitutes the bulk of comet Wild 2 (Brownlee et al. 2006; Nakamura et al. 2008). However, hydrous phases such as serpentine or phases precipitated from hydrothermal fluids are notably absent from the reported comet Wild 2 inventory and this is unexpected because chondrites and IDPs carry widespread evidence for hydrothermal action.

The Wild 2 results show similarities with known extraterrestrial materials, but there are also differences. Ishii et al. (2008) reviewed the mineralogical work carried out on comet Wild 2 to date and suggested that there were stronger similarities to asteroidal meteorites than to IDPs. Until the Stardust mission, IDPs have been our only source of cometary material (Rietmeijer 1998). Westphal et al. (2008) used X-ray absorption data (Fe-XANES) to show that Wild 2 tracks have a mixture of oxidized and reduced Fe that is broadly consistent with chondrite-like compositions but not clearly linked to any one known chondrite group. Joswiak et al. (2008) have shown the presence of Na-rich pyroxenes in 15 tracks, also with compositions distinct from those of known unequilibrated chondrites. Thus, the diversity of mineralogical assemblages present in comets is becoming apparent. GEMS (glass with embedded metal and sulfide), components that are characteristic of IDPs have also not been firmly identified or distinguished from molten aerogel (Zolensky et al. 2006).

Detailed mineralogical studies of the cometary grains distributed along the aerogel tracks (as distinct from terminal grains at the ends of tracks) have shown the importance of understanding the effects of collection such as heating and oxidation or reduction within the aerogel at 6.1 km s^{-1}. This is discussed in more detail in Grossemy et al. (2008) and Burchell and Kearsley (2009) and Burchell et al. (2006a). Briefly, Rietmeijer et al. (2008) and Leroux et al. (2008) used analytical TEM analyses of samples from along cometary tracks to show that the most frequent microstructure consists of a silica-rich glassy matrix containing a large number of vesicles and abundant Fe-Ni-S inclusions. This suggests that a large proportion of incoming dust particles were fully melted and mixed with molten aerogel. The larger particles toward the terminal ends of the aerogel tracks have preserved more of the pristine cometary material. This is in agreement with studies of laboratory analog samples where mineral projectiles grains of known composition were captured in aerogel using light-gas gun experiments (e.g., Noguchi et al. 2007; Hörz et al. 2008; Burchell et al. 2009).

In this article, we report on analysis of grains found in two tracks in the Stardust aerogel (both grains located along track walls and terminal grains). A variety of complementary analysis techniques have been used i.e., optical microscopy, SEM, microRaman, micro XRS fluorescence, and Fe-XANES, EXAFS. The focus of our work has been the identification of oxide phases in the samples and consideration of their possible origins.

SAMPLES AND METHODS

The track 41 keystone (from C2044,0,41,0,0) was cut and prepared at the University of California (Berkeley) (using the method described in Westphal et al. 2002). In the nomenclature of Hörz et al. (2006) and Burchell et al. (2008), track 41 is a Type B, ''turnip'' shaped track, where the particle has broken up during impact, producing a large cavity (lined with fine fragments of the impactor) in the upper half of the track. This cavity is accompanied by two styli, which emerge beneath the cavity, well aligned with the incident impact direction; terminal grains can be found at the end of these styli. The sample used here was a 4×2.5 mm transverse slice through the track, close (0.8 mm) to the track entrance (Fig. 1) and as such was a sample of cometary grains distributed along a track. The aerogel slice was placed between two glass slides with a depression within which the aerogel slice laid. An optical image of part of the aerogel slice, showing one of the several captured grains, is shown in Fig. 2.

Track 121 is shown in Fig. 3 and is a Type A, ''carrot'' shaped track. Track 121 was recovered from a chip that fell off C2005 during the tile removal process. There appears to have been relatively little initial disaggregation of the incident particle during capture in the coma and terminal grains are present at the end of the track. Gold mounts for the terminal particles from track 121 were prepared at the Open University (UK). These were sent to NASA JSC and microtomed sections of track 121 samples (C2005,2,121, 1,0 and C2005,2,121,2,0) placed onto the Au mounts and returned to the UK for analysis.

In parallel to the Stardust samples, laboratory analog samples were prepared using the two stage light-gas gun at

Fig. 1. Track 41. This is a Type B "turnip" shaped track of length ~4 mm and the impact was from the left of the image moving right. It was removed from the cometary collector cell 44. (See Burchell et al. 2008 for a discussion of track nomenclature and the distribution of tracks in the collector tray. An extended discussion of the characteristics of Type B tracks is given in Trigo-Rodríguez et al. 2008.). Our slice was cut 0.8 mm in (gray vertical rectangle) from the track entrance. Track image courtesy of NASA JSC.

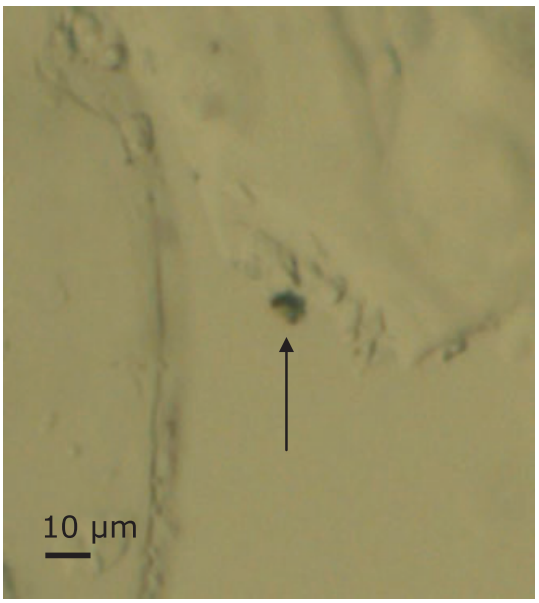

Fig. 2. Optical image of selected region of C2044,0,41 (transverse slice from track 41, see Fig. 1; also arrowed in the area Rm in Fig. 11a). Shown arrowed is a grain captured in the aerogel on the wall of the track cavity (the bottom right quadrant of the figure is the track cavity, the other three quadrants are part of the extracted aerogel slice).

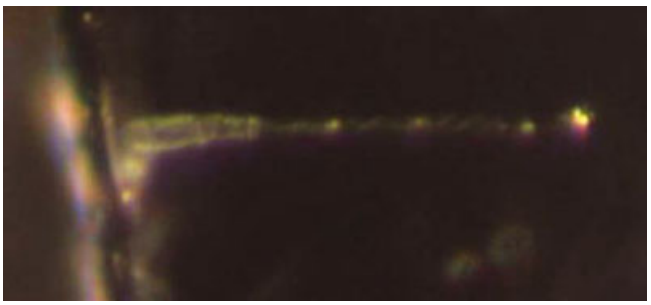

Fig. 3. Track 121. This is a Type A "carrot" shaped track of length ~0.9 mm and the impact was from the left of the image moving right. It was taken from a chip off the cometary collector cell 5. The terminal grains used here were removed from the end of the track (bright region at right hand side of image). Image courtesy of NASA JSC.

Table 1. Analog aerogel samples used in this work.

Mineral	Grain size (μm)	Aerogel density (kg/m^3)	Impact speed (km s^{-1})
Hematite (Kent sample)	10	32	6.17
Magnetite (BM-2005 M316)	10	27	5.94

the University of Kent. This gun (Burchell et al. 1999) was used to fire samples of mineral grains of known composition at standard aerogel samples. Unlike the Stardust aerogel (3 cm deep blocks, some of which had a density which varied from 5 kg/m^3 at the front face to 50 kg/m^3 at the rear surface; other cells had no significant density gradient), these laboratory samples all had a fixed density (27–30 kg/m^3) throughout which was chosen to be similar to the nominal Stardust density gradient. Minerals used were hematite and magnetite. Details of the samples are given in Table 1.

The analyses were planned to minimize the effects of sample damage on our mineralogical characterization. Reflected light photography and microRaman analyses were performed before our SEM analyses and synchrotron work. Track 41 was analyzed by micro-Raman and synchrotron radiation, the track 121 terminal samples by microRaman then SEM.

Raman Analyses at Kent and Open University

The use of Raman spectroscopy to successfully identify mineral grains captured in aerogel was demonstrated by Burchell et al. (2001) for olivine and enstatite. Subsequent work showed that a wide range of minerals could be identified with grain sizes down to 5 μm (Burchell et al. 2006b). Once a Raman waveshift spectrum has been obtained (and the slowly varying

broad background subtracted where necessary), the remaining relatively narrow peaks can be used to identify minerals. In this work, a point Raman spectrometer was used at the University of Kent to study C2044,0,41,0,0 and C2005,2,121,2,0.

The Kent microRaman system was integrated into an Olympus BX40 microscope. The Raman module was a Jobin Yvon microRaman module, with a HR640 spectrograph with a CCD (liquid nitrogen cooled). Dispersion on the CCD was about 0.5/cm per pixel. The illumination was from a He-Ne laser (632.8 nm). The full width of the laser spot size was about 3–5 μm and the maximum laser power at the sample was about 10 mW. Such a power density can be sufficient to induce significantly elevated temperatures in samples unless the heat can be conducted away efficiently.

Aerogel is a poor heat conductor, so care has to be taken to avoid excessive heating effects from laser illumination when examining small particles captured in aerogel, using laser illumination at ~750 W/mm^2 maximum power. This is discussed in Burchell et al. (2006b) where, using the same microRaman system as here, elevated temperatures of typically 100–160 °C were found for small (10–50 μm) mineral grains captured in aerogel. These results were found to depend on the absorption power of the minerals. Olivine showed modest (20 °C) increases in temperature during laser illumination, silicon carbide had a greater temperature (180 °C) and one initially unknown mineral grain (subsequently identified as vanadium pentoxide by comparison with similar spectra in the literature, e.g., Zhou and He 2008) gave a temperature of 480 °C. These temperatures were estimated from Stokes-anti-Stokes line ratios in the Raman shift spectra. For particles, which fluoresce, higher temperatures were found on average. For example, ruby grains in aerogel showed temperatures of typically 20 to 230 °C, while one grain (out of 15) had an elevated temperature under full laser illumination of ~700 °C, thus showing that, even in a sample of one material, small variations in composition or conditions inside the aerogel can result in substantial changes in heating under laser illumination. Bearing these effects in mind, a series of filters were used to attenuate the laser illumination during the analysis. The lowest filter had only 8% transmission at the laser wavelength, and all analysis commenced with this in use. Sample temperature was monitored by using ratios of Stokes and anti-Stokes lines as described previously (Burchell et al. 2006b). When analyzing Raman spectra, fitting was performed using the GRAMS/32 (galactic) package with an assumed Lorenztian line-shape for each peak.

Laser Raman microprobe analyses of particle C2005,2,121,1,0 were performed at the Open University. Integration times of a few minutes using a 60 μW, 514-nm laser, and a 1.5-micron spot resolution were employed. This gave 24 W/mm^2 power density, which owing to the relatively short integration times e.g., compared with some of our other Raman analyses, minimized the risk of sample damage.

SEM Analyses

Following the microRaman analyses, the track 121 terminal samples were studied with an FEI Sirion Field Emission Gun SEM (FEG-SEM) and a Philips XL30 Environmental SEM at UL. The FEG-SEM was operated at 4–9 keV and a beam current of 400 pA for imaging. Qualitative EDS point analyses were performed at 12.5–15 keV, ≤650 pA beam current with a PGT EDS system on the FEG-SEM. Beam currents were measured on a Faraday cup. The ESEM (with Link EDS) was used at 1 torr pressure when sample charging on C2005,2,121,2,0 occurred during some analyses using the FEG-SEM. This was found to overcome the majority of charging problems. EDS analysis times ranged from 50–1000 s for point analyses depending on our assessment of sample charging, potential damage, and elemental concentrations. For C2005,2,121,2,0 individual spectrum X-ray counts from across the sample were added together to produce a representative spectrum.

FIB and TEM Analysis

After identification by SEM of iron oxide grains within a terminal area of Track 121 (C2005,2,121,2,0), a technique was developed for extraction of one of the grains for TEM analysis. An FEI Quanta 3-D focused ion beam scanning electron microscope (FIB-SEM) was used at UL for sample preparation: milling an approximately 120 nm thick wafer containing a cross section of one of the iron oxide grains. The FIB-SEM Ga^+ ion beam used for the milling was operated at 30 kV accelerating voltage. Prior to application of the run script, the particle was capped with a 10×2.5 μm carbon layer approximately 150 nm thick followed by Pt of equivalent dimensions in order to protect the Fe oxide grain from the effects of the ion beam. Both layers were deposited via electron beam deposition using the gas injection system (GIS). The conventional 15×4 μm TEM runscript was amended to produce a 5×4 μm sample wafer dimensions required miniaturization in order to preserve the rest of the terminal mass. A 120 nm thick wafer was produced to ensure that the particle cross section would remain intact. The wafers were imaged with secondary electron snap shots at sequential stages of the milling process and the runscript was aborted before the final milling currents in order to help preserve the wafer. Manual thinning was

applied post extraction with low beam currents < 100 pA to ensure electron transparency of the grain. The wafer was extracted in situ using the Omniprobe lift out mechanism, and attached to a copper grid using carbon welding with the GIS and ion beam at 20 kV.

A JEOL 1200 TEM with a PGT EDS system was used for analysis of the extracted grain. Its LaB_6 thermionic source was operated at 200 kV and 111 μA emission current. Bright field imaging, STEM EDS, and selected area electron diffraction (SAED) were performed on the particle and surrounding gold foil mount. STEM EDS analyses were performed at 14 points in and around the iron oxide grain for 50 s each and X-ray mapping was performed with STEM mode for 2 h.

In order to check that the Ga^+ ions in the FIB did not create amorphous Fe oxides, we conducted FIB-SEM analyses of magnetite-bearing symplectites in nakhlite meteorites (Changela and Bridges 2009). The preservation of the magnetite and other phases showed that FIB-SEM analyses did not change the structure of the FeO studied in our Stardust samples.

MicroFocus XRS, XANES and EXAFS

Microfocus XRS and XANES spectroscopy was performed at Beamline I18 of the Diamond Light Source, Oxfordshire. This beamline operates from a 3 GeV synchrotron with typical currents of 200 mA. A Si (1 1 1) and (3 1 1) double crystal monochromator was used for energy selection with resolutions of 10^{-4} and 10^{-5}, respectively. A 9 element germanium based solid state detector was used which is capable of measuring the X-rays of Ca upwards. Energy calibrations are regularly checked on I18 with Mn metal samples.

Microfocus XRS (fluorescence) maps were generated at three areas of the transverse slice of track 41 (C2044, 10, 41, 0, 0). The germanium fluorescence detector was placed 45° to the sample with the beryllium window as close as possible to maximize count rates. 250 × 250 μm maps were produced at 13 keV and a dwell time of 5 s. Beam spot sizes were 3–4 μm. Long integration times of 500 s were performed on hotspots identified after mapping. At characteristic energies, called absorption edges, the X-ray absorption of an element changes markedly. Near an absorption edge, the spectra may contain fine structure that reveals information about valency, the electronic and geometrical environment of the absorbing atom. Fe K edge X-ray absorption near edge structure (XANES) was performed on hotspots. Approximately 120 data points were integrated across the XANES pre and post Fe edge. One second integration was performed at each 0.2–0.4 eV energy step from 6962–7090 eV, followed by 5 s onwards beyond the Fe K edge extended X-ray absorption fine structure (EXAFS) up to 7500 eV. However, this region was too noisy for successful fitting to the co-ordination environment for track 41 and so our mineral identifications are based on XANES. A range of mineral standards similar to the phases studied were also analyzed: magnetite (Fe_2O_3FeO), hematite (Fe_2O_3), Mg-rich olivine from the Admire pallasite meteorite (Mg/Mg + Fe atomic ratio 0.88), chromite $FeCr_2O_4$, Fe-sulfide–pyrrhotite ($Fe_{1-x}S$). They were powdered with an agate mortar and pestle and mixed with boron nitride powder at 5 mg to 95 mg proportions, the pellets were then used for XANES. Samples and standard powders were mounted on low X-ray absorption tape to preserve their integrity and using this tape, together with the thin aerogel within which the cometary tracks lie, means that X-ray absorption effects for elements with Z ≥ Ca were small enough to ignore in this work. XANES spectra were reduced using *Pyspline* software (Diamond Light Source, Oxfordshire, UK), XRS data with *PyMCA* software. The resultant XANES spectra were normalized by the software to the EXAFS region. The Berkeley XANES spectral library was also used to compare with our XANES results.

RESULTS

SEM and TEM of Terminal Areas of Track 121

C2005,2,121,1,0

This sample consists of a 10 × 10 μm mixture of glassy aerogel and a few percent of cometary grains. The relatively smooth surface texture and compositional analyses suggest that this part of track 121 has undergone some melting during capture heating. Spot analyses showed that there is a high concentration of iron oxide grains (Fig. 4). These appear to be pure Fe oxide; despite long acquisition times on numerous spots most grains had no other detectable elements except Fe, O with Au, Al, Si resulting from the substrate and aerogel. As some glassy aerogel was attached to the iron oxides, grain sizes were difficult to measure accurately but ranged up to approximately 100–200 nm. A second elemental signature for some grains was Mg-Fe-O-(Si), consistent with the common presence of forsterite olivine in many of the Stardust samples and characteristic of silica-rich glass in the Stardust samples (Zolensky et al. 2006; Leroux et al. 2008; Rietmeijer et al. 2008).

Following SEM characterization, an Fe oxide grain was extracted from this sample by FIB-SEM (see the section FIB and TEM Analysis) and analyzed by TEM (Fig. 4) in order to check its composition and determine its structure. Figure 4d shows an EDS spectrum taken from the grain. The Ga peak arises from some implantation

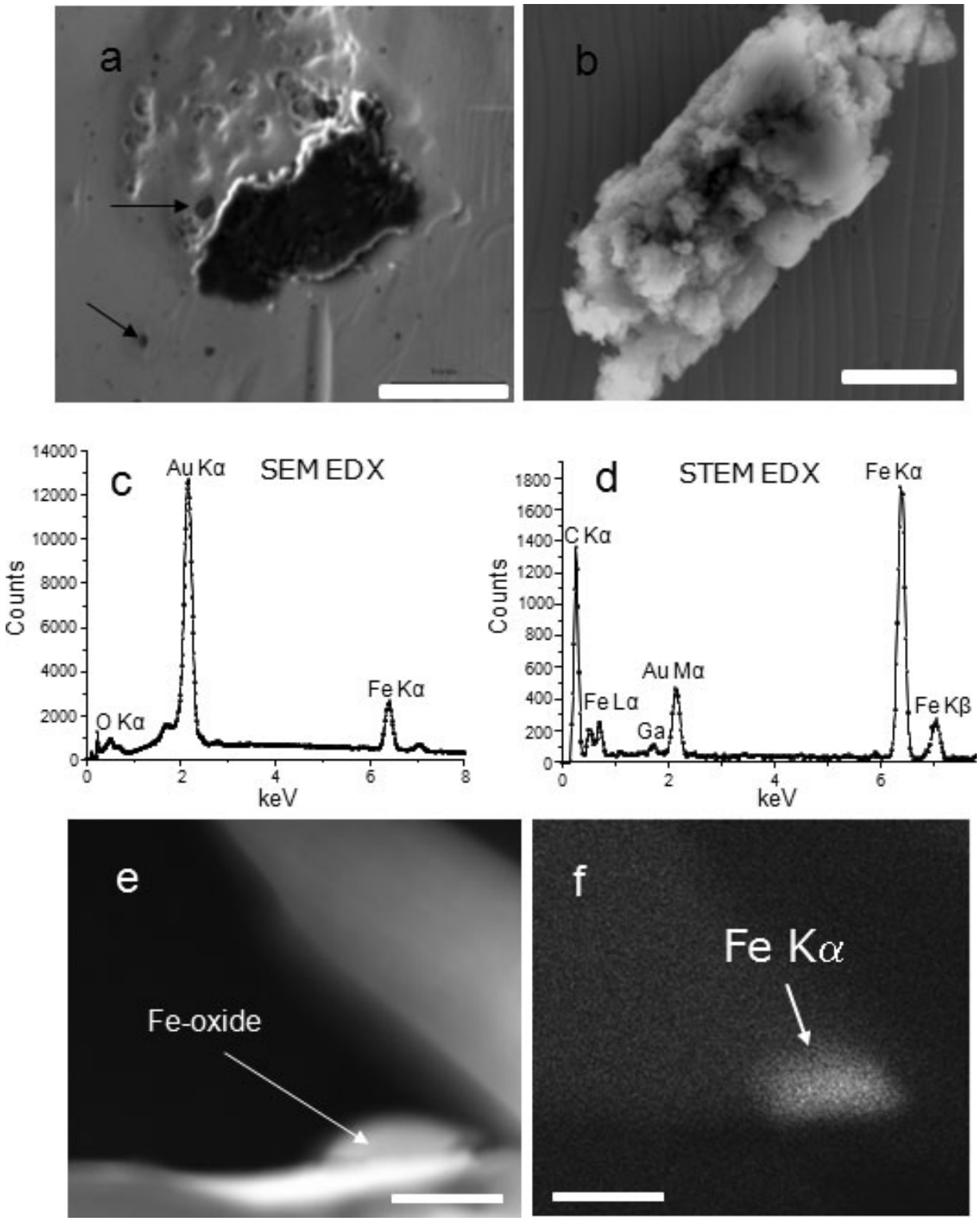

Fig. 4. a) SE image of terminal area of sample C2005,2,121,1,0 at 5 kV. Iron oxide (grains arrowed) has been found within and beside the terminal area of aerogel. Scale bar is 5 μm. b) SEM image of terminal area of C2005,2,121,2,0 at 9 kV. Scale bar is 5 μm. MicroRaman spectroscopy suggests the presence of magnetite-hematite. c) SEM EDX spectra of iron oxide grain in C2005,2,121,1,0. The Au peak is from the substrate on which the particle was pressed. d) 50 s integrated EDS spectra of an iron oxide grain in TEM after FIB extraction from C2005,2,121,1,0. e) STEM bright field image of wafer containing Fe oxide. Scale bar is 0.2 μm. f) EDS Fe Kα intensity map showing the location of the Fe-oxide, scale bar is 0.2 μm same field of view as (e).

during the ion milling process, the Au peak is due to excitation of some X-rays from the underlying mount.

Selected area electron diffraction of the Fe oxide grains showed the absence of any diffraction pattern and thus the oxide is structureless. The surrounding gold foil did, however, show diffraction demonstrating that it is the amorphous nature of the Fe oxide rather than the thickness of the extracted wafer that caused the lack of a diffraction pattern.

C2005,2,121,2,0

This sample consists of a 6×4 μm aggregate of aerogel and scattered cometary grains. Like the 121,1,0 sample it contained a dominant Fe signature (associated with iron oxide—see the Raman section below) from the cometary grains in addition to Si which is mainly produced from the aerogel (Fig. 4). However, the surrounding aerogel precluded imaging discrete grains. Subtracting the Au background from an X-ray spectra taken from the sample indicates, qualitatively, that it contains S as well as Fe and Mg. This suggests the presence of minor sulfides, although these have not been detected by microRaman, perhaps because of their small total volume. Such sub-micron grains could be fragments that were stripped off larger grains during capture. Unlike 121,1,0, this sample does not appear to have undergone melting.

Both 121,1,0 and 121,2,0 are samples of the terminal areas and thus iron oxides are present near the end of this track. A large single terminal grain has not been identified in these samples.

Raman

Raman analysis of the Stardust samples was carried out in addition to tests of standard sample materials.

Laboratory Analog Samples

Before considering the Stardust samples, the general case of magnetite (Fe_3O_4) and hematite (α-Fe_2O_3) under Raman analysis was considered. The Raman spectra of these minerals are distinct from other Fe oxides e.g., goethite and maghemite. Raman spectra were taken from raw grains of both magnetite and hematite (placed on microscope slides) using an 8% transmission filter to keep laser power on the samples low (see Fig. 5). The spectra obtained are typical of the spectra found in the literature for these minerals, e.g., de Faria et al. (1997) and the position and width of each peak are given in Table 2. For the hematite specimen (Kent micro-Raman), the series of seven sharp peaks, which extend up to 611/cm (what appears in the figure as a single peak at 293/cm is resolved by the fit into two narrow, just separable peaks), are similar to those reported in the literature typical of hematite and are typically assigned to the expected seven phonon lines for this material (e.g., see de Faria et al. 1997). The very weak peak at 661/cm is barely evident but is included for completeness. The peak at 1317/cm is also seen by other workers. It has been assigned to two-magnon scattering in the anti-ferromagnetic hematite (Martin et al. 1977), or more recently to an overtone of a Raman-inactive phonon (Massey et al. 1990). The magnetite spectra seen here are characterized by just two narrow sharp peaks

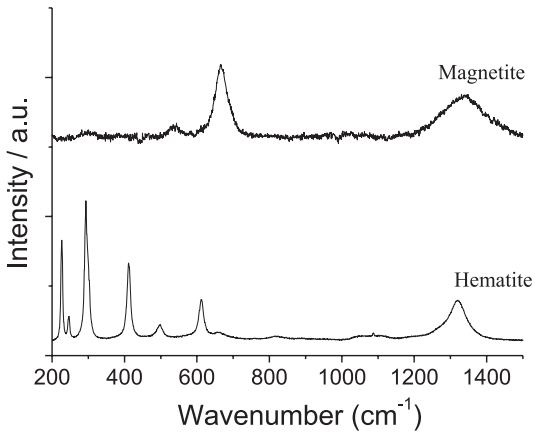

Fig. 5. Raman spectrum from raw grains of hematite and magnetite standards.

Table 2. Position and width of peaks in Raman shift spectra for samples in Table 1 and for laser heated magnetite.

	Peak positions and width (/cm)	
Sample	Raw grain	After capture in aerogel
Hematite	226.1, 4.9	218.9, 9.9
	245.9, 4.9	234.4, 6.6
	292.7, 7.2	282.9, 21.5
	299.8, 8.2	–
	411.4, 10.8	395.7, 22.8
	496.1, 19.3	478.3, 15.9
	611.7, 15.3	602.6, 51.9
	661.0, 28.7	665.6, 66.6
	1316.9, 56.9	1293.9, 79.0
Magnetite	536.9, 27.4	–
	667.2, 39.3	661.2, 45.0
	1337.0, 136.4	1323.6, 87.7
Magnetite (laser heated)	226.0, 5.6	–
	245.2, 5.7	–
	292.1, 8.0	–
	299.4, 8.8	–
	410.5, 12.6	–
	495.8, 22.4	–
	610.8, 16.4	–
	660.5, 29.4	–
	1316.4, 77.5	–

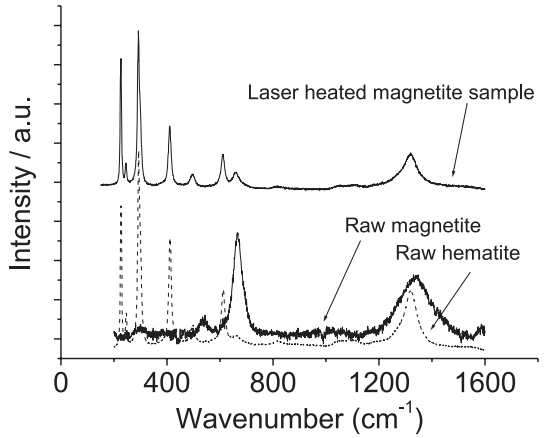

Fig. 6. Raman spectrum (upper trace) from a raw grain of magnetite illuminated at high laser power (i.e., heated to high temperature). The two lower traces are for raw grains of magnetite (solid line) and hematite (dashed line) taken at low laser power. The upper trace (peak positions and widths are given in Table 2) can be seen to be a combination of the two lower traces, with the hematite contribution dominating.

(537 and 667/cm) and a broad peak at 1337/cm. There is some discussion in the literature (e.g., de Faria et al. 1997) as to whether the latter peak is in fact associated with magnetite or represents the presence of hematite contaminants in the samples. Here we find that it has a different peak position and width to the peak seen in the hematite at 1317/cm.

As has been pointed out by several authors (e.g., de Faria et al. 1997; Shebanova and Lazor 2003) that laser heating of magnetite samples (to 240 °C) during Raman analysis causes the appearance of bands in the Raman spectra that are associated with hematite, reflecting an irreversible temperature induced transition from magnetite to hematite at around 240 °C. This is illustrated here in Fig. 6 where 88% of full laser power (i.e., 8.8 mW) was used to heat a magnetite sample to 205 ± 20 °C and take Raman spectra from it (peak positions and widths are given in Table 2). In the Raman spectrum from the heated sample, the characteristic bands of hematite at low wave shift number are now apparent, along with (and stronger than) those for magnetite. At ~1300/cm, the peak observed in the hematite sample has now replaced the broader and slightly higher wave number peak in the original magnetite spectrum (Fig. 5). This indicates that the grain has been heat processed by the laser during Raman analysis and (at the particle's surface) is now a mixture of hematite and magnetite.

This raises issues with regard to heating during analysis. Firstly, does heating during capture in aerogel alter the samples? As discussed later, there is evidence that peak projectile temperatures during capture in

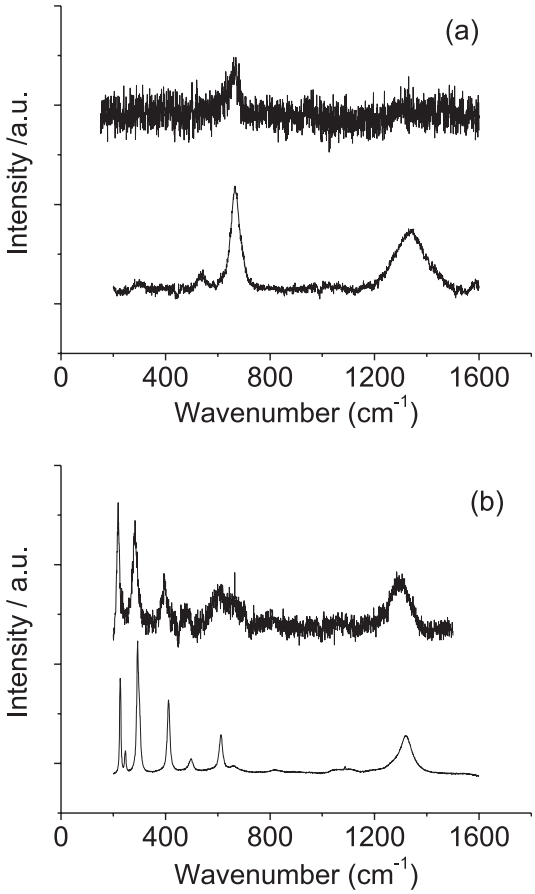

Fig. 7. Raman spectra of (a) 10 μm magnetite and (b) 10 μm hematite grain after capture in aerogel (density 30 kg/m^3) at 6.1 km s^{-1}. In each case, the upper spectrum is in aerogel and the lower trace is from a raw grain for comparison; the characteristic peaks of each raw sample are still present after capture (and are listed in Table 2).

aerogel can reach as high as 2040 °C. In addition, Noguchi et al. (2007) report elevated temperatures, and made TEM observations of mineralogical changes in samples captured in aerogel which are associated with transition temperatures of 500 °C (i.e., in excess of those needed for the magnetite to hematite transition at low oxygen fugacities). These elevated temperatures were found in a surface layer 1–2 μm thick of captured grains, whose interiors showed significantly less heating. Secondly, we must also consider that, even when low laser power is used, the heating effects due to the Raman laser illumination may be exacerbated for small grains captured in aerogel due to aerogel's poor heat conduction properties (particularly for long integration times).

Raman spectra were obtained at low laser power (i.e., with the 8% transmission filter) from the mineral grains captured in the laboratory aerogel samples described in Table 1 and Fig. 7. For magnetite (Fig. 7a),

it can be seen (Table 2) that the main characteristic peak is shifted in position by 6/cm. The broad peak at 1324/cm is barely above the noise in the spectra and by itself would probably not trigger a peak identification. The increased signal to noise ratio in the spectra is due to the grains being observed through a thickness of aerogel (2 mm in this case, much greater than the Stardust sample analyzed below) and this is common in Raman studies of grains in aerogel. For the hematite sample, the characteristic peaks are still strongly visible after capture, albeit again with an apparent slight downward shift in peak position and increased widths (similar shifts and broadening have been reported previously when samples are heated e.g., see Shebanova and Lazor 2003). This increased width explains the inability to resolve clearly the two peaks expected at 293 and 299/cm and their appearance as a single peak. The grains used in taking these spectra were 10 μm in size, similar within a factor of 2 to the Stardust grains that were analyzed (e.g., Fig. 2). The important conclusions of these experiments are that the acquisition of Raman spectra does not thermally process iron oxide grains sufficiently to entirely change magnetite into hematite.

As a further check, Raman spectra were taken for long (20 h) periods, at full laser power (10 mW) on magnetite grains captured in aerogel. Grains about 30 μm in size were chosen which were near the surface of the aerogel and which were about 30 μm in size. These laser illumination conditions exceeded those used to analyze any of the comet Wild 2 samples. The resulting Raman wave shift spectra are shown in Fig. 8. A range of results is apparent. In one case (Fig. 8a), the spectrum was altered, such that it was dominated by the peaks expected from hematite, with only weak magnetite peaks remaining. In the other case (Fig. 8b), the spectrum was still dominated by the peaks associated with magnetite. Based on ratios of anti-Stokes and Stokes lines in the Raman spectra, we associate a temperature of 216 ± 20 °C with the sample in Fig. 8a and 206 ± 20 °C with that in Fig. 8b. We hypothesize that the conditions under which the samples were analyzed may have varied slightly, resulting in the slightly different temperatures in each sample (albeit within our measurement uncertainty) and that the transformation process may be very sensitive to temperature at around 200 °C. This wide variation in outcomes suggests that the results of long duration Raman analysis with high laser power on small grains in aerogel need to be interpreted with caution. The presence of peaks associated with magnetite is indicative of the presence of that mineral in the original sample, but the strength of the peaks does not necessarily indicate the abundance of magnetite that was originally present. Any hematite peaks from a long duration analysis could be interpreted as due to heating and partial alteration during the Raman analysis, rather than necessarily being indicative of the presence of hematite pre-analysis.

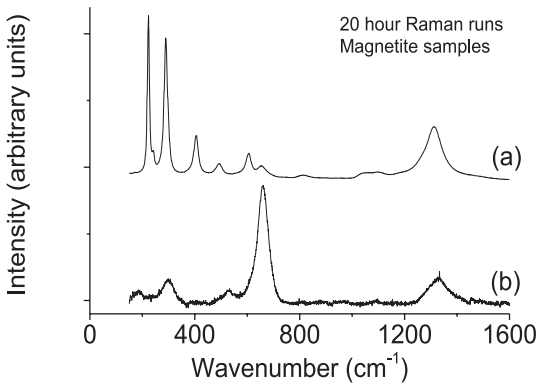

Fig. 8. Raman spectra from magnetite grains fired into aerogel at 6 km s^{-1}. The laser illumination was at full power for 20 h. Two grains were used. Before these long runs, the grains, when illuminated for short periods at lower laser intensity, gave magnetite spectra similar to that in Fig. 5. After the 20 h illumination, grain (a) is now mostly showing the spectrum associated with hematite, with weak magnetite peaks, whereas the spectrum for grain (b) is still dominated by the peaks from the original magnetite spectrum.

Track Slice C2044,0,41,0,0

The slice of Stardust track C2044,0,41,0,0 was examined optically and around the wall of the cavity several grains in the size range 5–10 μm were identified. Most gave no Raman signal (with laser power attenuated by the 8% filter to avoid any risk of damaging the sample), but one (shown arrowed in Figs. 2 and 11) did. To obtain a better signal to noise ratio in the spectra, this sample was illuminated at full laser power (10 mW) for 15 h. During this run, a full Stokes and anti-Stokes spectrum was obtained and the sample temperature during analysis was estimated as 209 ± 20 °C. The resulting Raman spectrum is shown in Fig. 9 with peak positions and widths given in Table 3. The spectrum is very similar to that from the hematite grains that did not undergo long duration analysis. The low wave shift number peaks are present, although the peak in the standard raw grains at just above 1300/cm is not totally distinct above the background. We can also see that the structure at just above 600/cm contains two peaks; one at ~610/cm is compatible with the hematite standard spectra, but the other at ~630/cm is similar to that found in magnetite. The lack of a peak above 1300/cm is not explained—as it is expected if hematite is present—but apart from this discrepancy, the best explanation of the spectrum is a combination of hematite and magnetite

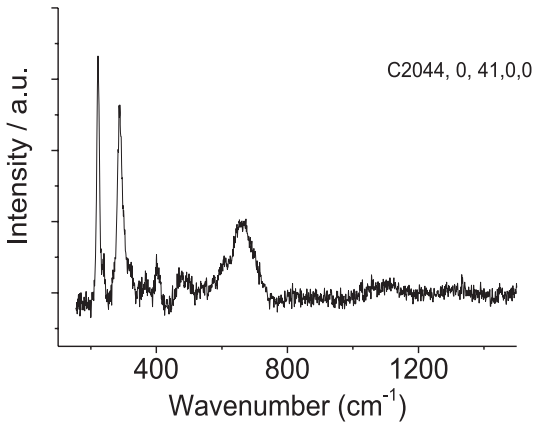

Fig. 9. Raman spectra from Stardust sample C2044,0,41,0,0 (track 41). The peak positions and widths are given in Table 3. By comparison with Fig. 5 (and Table 2), it can be seen that peaks characteristic of both magnetite and hematite are present (with the exception of the absence of a peak at around 1300–1340/cm).

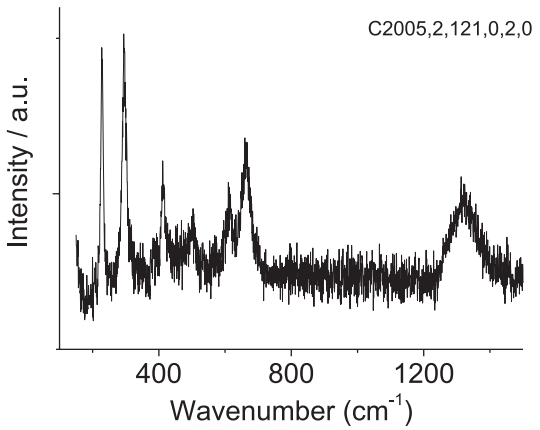

Fig. 10. Raman spectra from Stardust sample C2005,2,121,0,2,0 (a track 121 sample). The peak positions and widths are given in Table 3. By comparison with Fig. 5 (and Table 2), it can be seen that peaks characteristic of both magnetite and hematite are present.

Table 3. Position and width of peaks in Raman shift spectra for Stardust samples.

Sample	Peak positions, width (/cm)
C2044,0,41,0,0	222.0, 8.3
	288.9, 19.5
	401.4, 16.2
	482.9, 31.8
	604.1, 59.7
	664.1, 64.0
C2005,2,121,0,2,0	228.3, 8.0
	295.5, 13.9
	413.5, 17.3
	612.4, 16.4
	663.1, 27.0
	1323.7, 102

(with the qualifications given above about the possible consequences of heat processing of magnetite grains in aerogel as a result of long laser illumination at high powers). This is discussed further below.

Terminal Samples C2005,2,121,2,0 and C2005,2,121,1,0

Raman spectra were taken from one of the terminal grains in track 121 (C2005, 2, 121, 2, 0) and an example is shown in Fig. 10 (peak positions and widths are given in Table 3). Laser power was 8–44% of the total (0.8–4.4 mW), with illumination for 8 min in total on any one grain. At wave numbers up to just above 600/cm, the peaks typical of hematite were all visible. However, above this, the two peaks indicative of magnetite were also visible in the same spectrum. The peak at 663/cm is clearly distinct from the hematite standard peak at 612/cm but agrees well with that for magnetite. Also, the peak at 1324/cm has a peak position that is too high a peak position and is too broad to be associated with that in the standard hematite spectrum, but matches better with the magnetite standard. The best interpretation of the spectra is thus again a mixture of hematite and magnetite. The laser-induced heating effects in these samples were small; it was difficult to identify the anti-Stokes lines above the background noise level and we thus find that the sample temperatures during the Raman analysis were ≤87 °C.

Sample C2005,2,121,1,0 analyzed at the OU Raman gave no Raman signature of mineral structures. This is consistent with the amorphous nature of this Fe oxide as determined by electron diffraction.

X-Ray Microfocus Spectroscopy—XRF and XANES-EXAFS of Track 41

The track 41 slice was found to contain a range of different minerals and oxidation states. The grains are scattered around the track's bulb margin. X-ray Spectrometry (Fig. 11) showed Fe hotspots, Fe-Ni compounds, Fe-Ti (oxide—e.g., ilmenite), Cr-Fe-V-Ti-Mn (oxide-chromite), and an unidentified Fe-Zn compound (which may well be an aerogel contaminant, see below). Chromite has previously been identified in Wild 2 material e.g., in Al foil crater residues (Bridges et al. 2007). The detectable presence of V and relatively high Ti contents in the chromite are significant because this is characteristic of extraterrestrial (chondritic) chromite rather than terrestrial chromite (Alwmark and

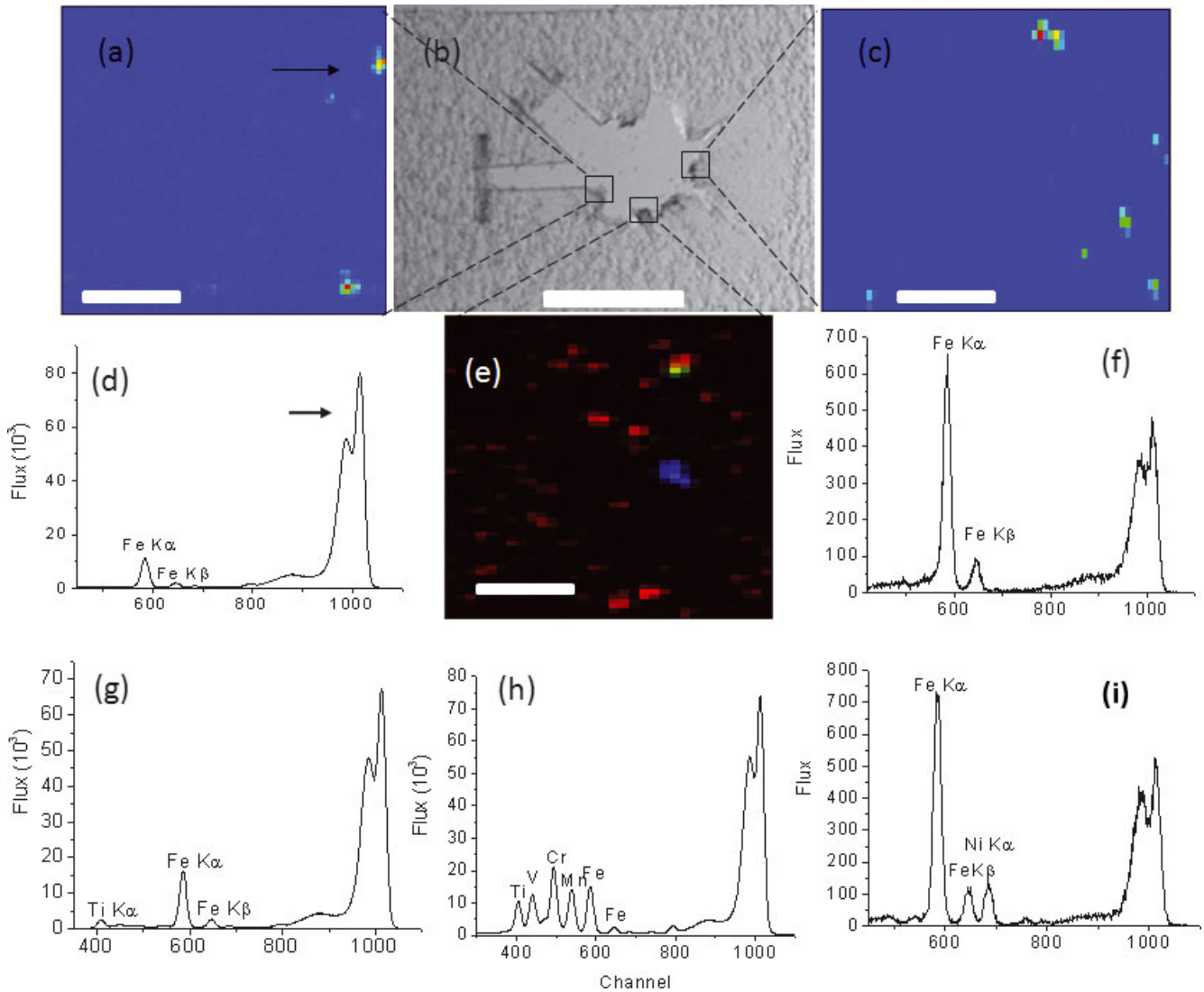

Fig. 11. XRS mapping of C2044,0,41 (track 41) using synchrotron X-rays. Note that the horizontal channel scale of the spectra does not correspond exactly to a keV scale although the relative positions of the characteristic peaks are accurate. a) Reflected light microscope image of transverse slice of track 41. The central, roughly circular hole is the track cavity. The rectangular channels are artifacts made by the mounting forks used to hold the sample during extraction from the aerogel tile. The slice is 300 μm thick. Scale bar is 1 mm. Mapped areas b–d and area with Raman analysis RM on hematite-magnetite grains shown. b) Fe Kα map, each pixel measures approximately 4 × 4.5 μm, showing numerous grains approximately 10 μm in diameter. Scale 80 μm. The most commonly found spectra found at the Fe hotspots are shown in d, f. c) Fe Kα map, which was also very similar to the Ni window (not shown here). Most hot spots in this area show a Fe-Ni-bearing composition displayed in i. d) "Fe- hotspot" spectra showing Fe Kα peak. The peak at channel no. 1000 is the scattering peak of the primary beam. e) RGB intensity map of another position of Track 41, indicating Fe (red), Cr (green) and Zn (blue) hotspots. f) Typical "Fe- hotspot" spectra showing Fe Kα peaks. The peak at channel no. 1000 is the scattering peak of the primary beam. g) Fe-Ti hotspot (ilmenite?) which is adjacent to the Fe-Cr-V-Ti-Mn hotspot. h) Cr hotspot—V-rich chromite (green in RGB). The V intensity peak is greater than that of Ti. V enrichment is a characteristic of extraterrestrial chromite (i) Typical Fe, Ni spectrum from map c.

Schmitz 2006). In this sample the chromite and Fe-Ti oxide were adjacent grains (Fig. 11).

Fe-XANES analyses (Figs. 12a–c) show that Fe hotspots have a marked absorption peak at 7110–7111 eV, before the main K edge. Another peak associated with ferric oxide occurs at around 7185 eV (Fig. 12b). Similar effects have been reported elsewhere for ferric oxide-bearing phases e.g., Prietzel et al. (2007). This pattern effectively rules out pyrrhotite and olivine as the mineral identities. The Fe hotspot patterns are very close to that of the magnetite (absorption peak at 7110 eV) and hematite standards (absorption peak at

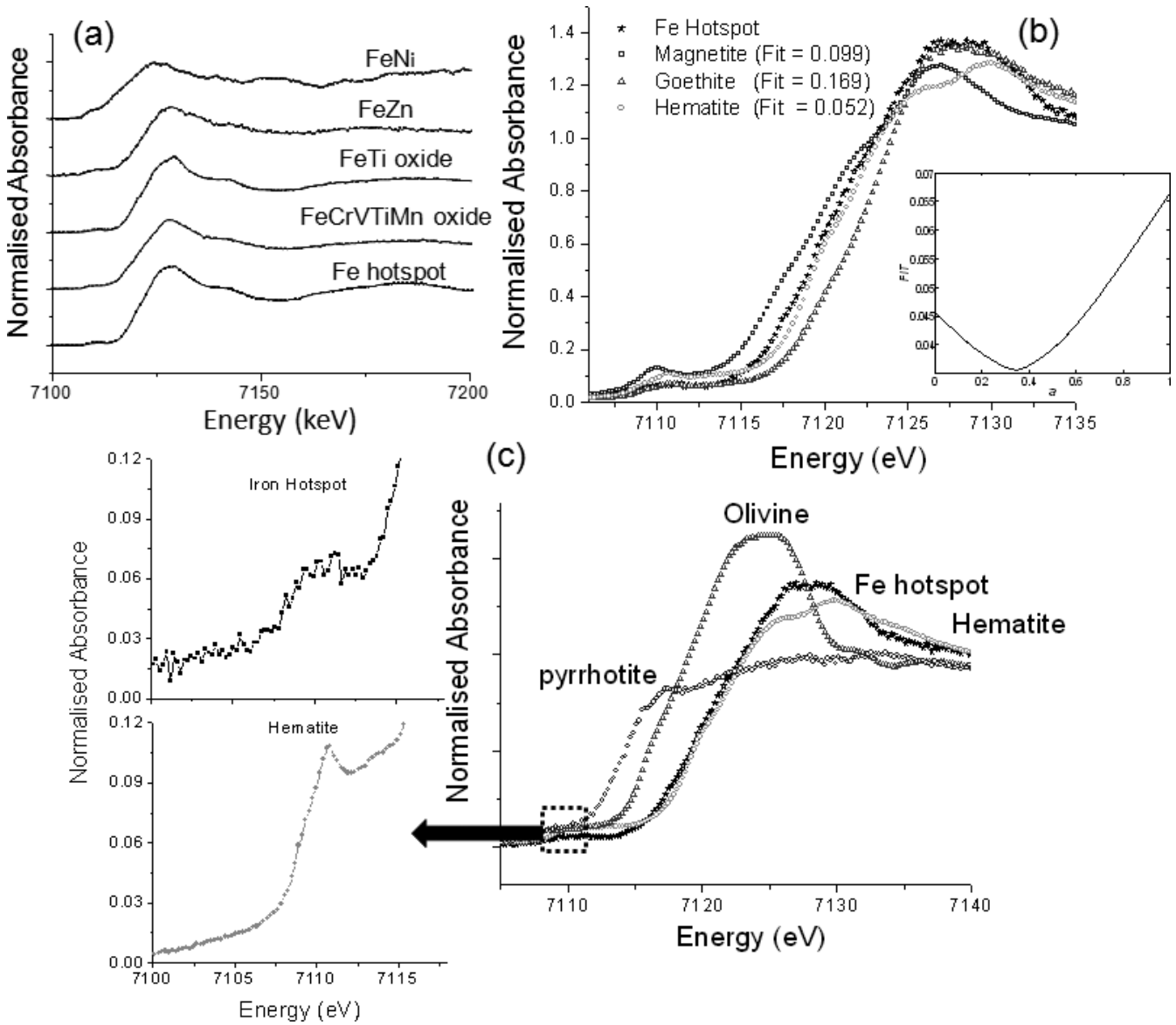

Fig. 12. Fe-XANES of minerals in track 41 and standards. 0.2–0.4 eV energy steps. a) Fe-bearing phases within track 41. A small absorbance feature around 7110–7112 eV (before the main absorption edges) is arrowed, which shows the presence of ferric oxide in all the samples, including the relict FeNi metal and the Fe-Zn contaminant phase. The relict FeNi metal also has an absorbance feature around 7160 eV, a feature characteristic of metal (Pingitore et al. 2002). b) Comparison between goethite FeOOH, hematite Fe_2O_3, magnetite Fe_2O_3FeO standards with Fe hotspots. The main absorption edges (7115–7125 eV) have a similar gradient for all the samples and are consistent with the presence of ferric oxide. The inset diagram shows a best fit calculated between the two spectra—hematite and magnetite—that are most similar to the Fe hotspot spectra and are consistent with the microRaman data. Simple fit calculated by Fe—[(1-a)magnetite + a.hematite]. The typical Fe hotspot shown is fit as a mixture of 38% magnetite, 62% hematite. c) Smaller energy range plotted to show the comparison between the Fe hotspot spectra and hematite. Plots (b) and (c) show that the Fe hotspot spectra are consistent with a mixture of magnetite and hematite and are not consistent with the presence of olivine or Fe sulfide (pyrrhotite). The olivine standard and Fe-sulfide standard both completely lack the peaks associated with ferric iron at 7110 eV and 7111 eV in magnetite, hematite, and the Fe hotspots.

7111 eV) and are consistent with a mixture of these two phases. To test this, we performed a simple fit between standards and sample (Fig. 12c) over the Fe-XANES edge and this suggests a mixture of 38% magnetite, 62% hematite in one of the sample grains. Fits to goethite around its Fe K edge were much poorer confirming the absence of this mineral.

Sulfur could not be analyzed by XRF with the Ge detectors but, by comparison with other work on Stardust samples (e.g., Leroux et al. 2008), it is possible

that sulfides could have been present. However, none of the XANES-EXAFS spectra in track 41 grains are consistent with an Fe-sulfide identity, sulfides being characterized by the absence of a marked absorption edge, e.g., pyrrhotite (Fig. 12c).

The Fe-Ni grain analyzed shows a marked absorbance feature around 7160 eV which distinguishes it from the hematite-magnetite mixes. A similar absorbance feature was noted in Fe metal by Pingitore et al. (2002). However, our sample also has an absorption peak around 7111 eV, which is consistent with a mixture of FeNi metal and ferric oxide. The Fe-Zn compound also shows this absorbance feature showing that it too has been oxidized to some extent.

DISCUSSION

Iron Oxides—Part of Comet Wild 2 or Relicts of Space Weathering, Terrestrial Contamination, Capture Heating and Analysis?

Irradiation of the comet's surface, the extreme thermal processing of the cometary dust during capture, some heating during analysis and terrestrial contamination during manufacture of the aerogel, all make interpretation of the original cometary assemblage difficult.

Space Weathering

Space weathering in lunar soils and asteroidal surfaces is manifested by nanophase metallic Fe (e.g., Pieters et al. 2000; Noble et al. 2007) within silicates. Farnham and Schleicher (2005) showed that Wild 2 had a reddened reflectance spectrum which suggests that space weathering has occurred on its surface. If this space weathered material is present, mixed in below the comet's surface and was carried by the jets from inside the comet into the coma then some of the nm-sized Fe-bearing particles e.g., in 121,1,0 might have originated as space weathered material on comet Wild 2. However, the O-bearing nature of the Fe-rich phases studied here requires that if space-weathered material was present it has undergone subsequent oxidation. The Fe-Ti and Fe-V-Mn-Ti-Cr oxide cannot have been derived through space weathering and instead we consider they are part of the original cometary mineral assemblage.

Capture Heating

During capture at 6.1 km s^{-1}, the cometary grains experienced substantial heating. After the first demonstration of capture of mineral grains at high speed in aerogel (Tsou et al. 1988), several studies of the effect of capture on mineral grains, quickly followed, including melting at grain surfaces (e.g., Bunch et al. 1991; Barrett et al. 1992) and these are summarized in Burchell et al. (2006a,b). More recent studies include Noguchi et al. (2007), Hörz et al. (2008), and Burchell et al. (2008). It is clear from the abundant melted, rounded Fe sulfide and metal grains found along the tracks that melting and sulfur remobilization has occurred in general. This can be seen for example, in the work of Leroux et al. 2008, who, as here, examined grains from track 41, along with grains from track 35 (a Type B, bulbous track), and track 44 (a large feature where the incident particle hit both aerogel and the container wall) and some grains of unknown track type. Recrystallized sulfide-metal assemblages frequently occur as metal (kamacite) cores and sulfide (pyrrhotite) rims in grains that range in size from nm to < 100 nm diameter. Taenite also occurs. Temperatures associated with capture of the cometary grains and metal-sulfide recrystallization must have exceeded that of the Fe-Ni-S eutectic. This eutectic temperature increases with pressure and is at least 950–1000 °C and gives a minimum temperature during capture.

There have been conflicting arguments for whether capture heating in aerogel causes oxidation or reduction. Rietmeijer et al. (2008) described Fe silicides near the entrance of track 44: they suggested these resulted from the reduction of melted Fe-Ni sulfide grains. Marcus et al. (2008) also reported light-gas gun experiments where ferric iron had been reduced to ferrous compounds and considered that this was associated with capture heating in the presence of carbon within the aerogel. In contrast, Grossemy et al. (2008) used Fe-XANES to show that ferric iron-rich particles identified near the track mouth of Allende meteorite particle tracks in aerogel (shot with a light-gas gun) were the result of the oxidation of olivine. Our Fe-XANES spectra of FeNi metal suggests that some oxidation has occurred during capture heating within 1 mm of the track 41 entrance, in agreement with the conclusions of Grossemy et al. However, the relatively high abundance of magnetite within the Allende meteorite means that some of the magnetite in the Grossemy et al. experiments (and thus by analogy within our samples) might have been derived from the meteorite (or in our case comet Wild 2) rather than being due to capture-related oxidation of other minerals. Oxidation of FeNi metal after the samples were returned to Earth through interaction with the atmosphere is also a possibility which cannot be ruled out as contributing to the limited oxidation identified in our Fe-XANES analyses of the Fe-Ni grains.

Heating During Analysis

The Fe-XANES and Raman spectra obtained from grains in tracks 41 and 121 show evidence for mixtures of hematite and magnetite at scales < 3–5 μm spot size of the illumination laser in the Raman spectrometer and the synchrotron spot size. As discussed above, tests on

the laboratory analogs showed that both hematite and magnetite remained distinct after capture in aerogel at speeds of ~6 km s^{-1}, but that prolonged exposure to strong laser illumination of magnetite grains in aerogel could produce hematite. This may have been relevant to just one of the grains which underwent a long duration analysis (Figs. 2 and 11) in the track 41 sample, but not to the extracted terminal grains from track 121—both the magnetite-hematite mixtures and amorphous Fe oxide. We therefore suggest that, in most cases, the micron-scale hematite and magnetite grains are primordial cometary grains and are not artifacts of capture or analysis. We particularly also note that our XRS and Fe-XANES analyses identified magnetite-hematite in spots that had not been analyzed at all by microRaman, so we do not believe that the Raman analyses caused the formation of the observed Fe oxides.

Origin of the Fe Oxides

Although we consider the Fe-Cr-V-Ti to be unambiguously cometary in origin, the Fe oxide potentially has a more complex origin. Zn-bearing grains such as one identified in track 41 are a sign that there is some contamination from the manufacture of the aerogel (M. E. Zolensky, personal communication). As described above, we do not think that the Raman analyses formed the magnetite or amorphous Fe oxide, but it is possible that some of the hematite which partially replaces magnetite in a large grain in track 41 (Fig. 2) may be an analytical artifact. The Fe-XANES analyses suggest that capture heating in the aerogel has partially oxidized the outer parts of the FeNi metal grains. The intermixing of grains like Fe-Cr-V-Ti-Mn and Fe-Ti oxide around the track 41 slice with magnetite-hematite is consistent with the original cometary Fe-bearing oxides probably having been largely preserved. However, we do not yet have firm proof for the cometary origin of the hematite-magnetite and further studies are required to check this.

The amorphous Fe oxide in sample 121,1,0 from track 121 could have originated through slight oxidation during capture of metallic iron. The origin of this amorphous phase is uncertain and there is no firm evidence that it is not a terrestrial contaminant from aerogel manufacture, like the Zn-Fe compound in track 41. However, the 121,2,0 sample, also from track 121 does have a crystalline magnetite-hematite structure. Thus, the Fe oxides in tracks 41 and 121 have a variety of origins mainly related to the comet Wild 2 parent body and capture heating-oxidation with relatively minor effects from microRaman analyses and possible terrestrial contamination of amorphous Fe-oxide.

Comparisons to Chondrites and IDPs

Iron oxide is found in IDPs (Rietmeijer 1998) intergrown with phyllosilicates and is interpreted as having resulted from low temperature hydrothermal alteration on a cometary CI-like parent body (Keller et al. 1992) or other carbonaceous chondrite parent body. Rietmeijer (1998) and Bradley et al. (1996) suggested that some magnetite found as overgrowths on silicate and sulfide minerals was the result of the heating and oxidation of silicates during atmospheric entry. Bradley (1994a) reported an Fe-Ni grain with a magnetite rim in an IDP. This was interpreted as having resulted from energetic particle bombardment during its passage in space. However, subsequent descriptions of space weathering effects have shown that this process is more likely associated with reduction e.g., Noble et al. (2007). Zolensky and Lindstrom (1992) described magnetite in 12 chondritic IDPs. They suggested that magnetite around the outer margins of IDPs was formed by oxidation of the IDPs during atmospheric entry, but that magnetite within the centers of IDPs was primary.

Magnetite is present in CI, CV, oxidized CO, CM, and CR chondrites. Keller et al. (1992) and Brearley and Jones (1998) made the comparison between IDPs and CI chondrites because magnetite is one of the common signs of asteroidal alteration in this type of chondrite. Magnetite is the second most abundant phase in CI chondrites and has been described by Madsen et al. (1986), Morlok et al. (2006), Choi and Wasson (2003), and earlier work summarized in Brearley and Jones (1998). It occurs in a range of textures, but most commonly as 10–30 μm size subspherical aggregates. Fe_2O_3 as maghemite or hematite can also be present, although this could in turn be the product of magnetite oxidation (Haggerty and Baker 1967). CI magnetite is intergrown with phyllosilicates, particularly serpentine. If the magnetite now present in our comet Wild 2 samples originated through such alteration, it might be expected to be associated with phyllosilicates such as serpentine minerals. The lack of phyllosilicates might be due to dehydration and recrystallization during capture, although it remains an anomalous absence in the Wild 2 analyses to date. The composition of magnetite in CIs—like that identified in our C2005,2,121,1,0 sample—is essentially pure Fe_3O_4 (Brearley and Jones 1998).

The asteroidal alteration in chondrites is believed to have occurred between 2 and 15 Myr after the formation of CAIs, but there does not appear to be any narrow set of oxygen fugacities or fluid composition associated with it (Zolensky et al. 2008). Morlok et al. (2006) concluded that low temperature alteration, including magnetite, in CIs formed in a closed system,

where mineralogical differences in the lithologies reflected heterogeneities in the starting material. Although asteroidal alteration is one possible origin for magnetite in chondrite meteorites and IDPs the origin for the Wild 2 grains remains unclear.

Flynn (2008) used the result of 20 synchrotron analyses of tracks and fragments of tracks to suggest that the more volatile element abundances, e.g., Zn, Cu, showed an affinity to anhydrous porous IDPs but the more refractory elements, e.g., Ca to Fe, were closer to CI abundances. Thus, the Flynn analyses suggest there may be no easy, exclusive correlation between comet Wild 2 and either IDPs or CI chondrites. However, Ishii et al. (2008) noted that amorphous silicates with embedded metal and sulfide (known as GEMS) were a major constituent of anhydrous porous IDPs, but that the initial reports of these in comet Wild 2 samples were compatible with impact capture processing of the aerogel, rather than cometary GEMS of which there are currently no firm identifications in Wild 2. Furthermore, they noted that refractory minerals, CAIs, chondrules, and chondrule fragments are normally absent from, or exceedingly rare, in chondritic porous IDPs, but are found in almost all chondritic meteorites. Thus, Ishii et al. suggested that comet Wild 2 was most similar to chondritic material originating within the inner solar system.

Our results show an unequilibrated mixture of reduced (e.g., FeNi metal) and oxidized phases in close proximity within the tracks. These phases can be present in both types of planetary material—chondrite and IDP. In IDPs, FeNi metal is often associated with GEMS (Bradley 1994a, 1994b) although FeNi metal has also been identified in some asteroidal IDPs (Rietmeijer 2004). As discussed above, it has been suggested that GEMS are absent/not yet demonstrated in the Stardust samples. However, melted aerogel and its enclosed, rounded Fe-Ni-S grains can appear similar to GEMS, making identification difficult.

If the apparent absence of GEMS is genuine, then the Stardust samples including the Fe oxide ones studied here are most consistent with comet Wild 2 material being of a chondritic rather than IDP nature. However, more data are required from the Stardust samples before the origins of the different minerals including Fe oxides and the IDP versus chondritic analogies become clear.

CONCLUSIONS

We have conducted a suite of materials characterization analyses by Fe-XANES, TEM, and microRaman on cometary dust grains captured by the NASA Stardust space mission soon after ejection from comet 81P/Wild 2. This has been backed up by studies of analog samples created in light-gas gun experiments. We find:

1. We have identified iron oxides in a slice taken 0.8 mm along track 41 and some terminal samples from track 121. V-rich chromite (Fe-Cr-V-Ti-Mn oxide), Fe-Ti oxide (ilmenite?), and partially oxidized FeNi metal are present in track 41. The terminal samples from track 121 also contain traces of sulfide and Mg-rich silicate.
2. Fe oxide grains are either a magnetite-hematite mixture or have no structure detected by electron diffraction.
3. Fe-XANES shows that capture heating in the aerogel has led to partial oxidation of some phases, notably the FeNi metal. This does not appear to have had a significant effect on the magnetite-hematite. Our light-gas gun experiments on laboratory analog samples of Wild 2 mineral analogs at 6 km s^{-1} suggest that the temperatures reached during Raman analysis of many hours duration might have been sufficient to cause some alteration of the magnetite to hematite. However, apart potentially from one large grain, which we analyzed for a long time, we do not think our microRaman analyses changed the mineralogy of the Fe oxides.
4. Amorphous Fe oxide might either be a product of the capture-related or terrestrial atmospheric oxidation of metallic iron. Terrestrial contamination within the aerogel is also possible.
5. The oxides co-exist with reduced, metallic phases (partially oxidized due to capture or terrestrial alteration). This provides further evidence that this comet consists of a diverse mixture of unequilibrated mineral assemblages. Further work is required to assess the similarities with IDP or chondrite samples and to calculate accurate abundances.
6. Finally, we recommend that, when reporting analyses of Stardust samples, authors need to specify the track and sample catalog numbers, and also state the track type (A, B, etc.) and where along the track the sample grain(s) were located (wall of cavity, terminal grain, etc.). This is necessary to help build up a more consistent picture of the degree of (heat) processing and mixing with aerogel that has occurred during the capture event and the relation of the analyzed grains to the original cometary dust particle.

Acknowledgments—We thank the NASA Curatorial Facility for supplying the Stardust samples used in this work and preparing the terminal particles from track 121. Andrew Westphal and Christopher Snead of University of California (Berkeley) are thanked for preparing track 41 and providing track images.

Matthew Marcus, Sirine Fakra, and Andrew Westphal are also thanked for giving access to their Berkeley XANES mineral spectral database. This work was carried out with the support of the Diamond Light Source. Fred Mosselmans and Paul Quinn of Diamond are thanked for assistance with collecting the microfocus spectroscopy data. Michael Cole (Univ. of Kent) is thanked for operation of the light-gas gun. STFC (UK) is thanked for financial support and NJF thanks the University of Kent Alumni for financial support. Adrian Brearley, Frans Rietmeijer, Mike Zolensky, and an anonymous reviewer are thanked for their comments which improved the manuscript.

Editorial Handling—Dr. Adrian Brearley

REFERENCES

Alwmark C. and Schmitz B. 2006. Extraterrestrial chromite in the resurge deposits of the early Late Ordovician Lockne crater, Central Sweden. *Earth and Planetary Science Letters* 253:291–303.

Barrett R. A., Zolensky M. E., Hörz F., Lindstrom D. J., and Gibson E. K. 1992. Suitability of silica aerogel as a capture medium for interplanetary dust. Proceedings, 22nd Lunar and Planetary Science Conference. pp. 203–212.

Bradley J. P. 1994a. Nanometre scale mineralogy and petrography of fine-grained aggregates in anhydrous interplanetary dust particles. *Geochimica et Cosmochimica Acta* 58:2123–2134.

Bradley J. P. 1994b. Chemically anomalous, preaccretionally irradiated grains in interplanetary dust from comets. *Science* 265:925–929.

Bradley J. P., Keller L. P., Brownlee D. E., and Thomas K. L. 1996. Reflectance spectroscopy of interplanetary dust particles. *Meteoritics & Planetary Science* 31:394–402.

Brearley A. J. and Jones R. H. 1998. Chondritic meteorites. In *Planetary materials*, edited by Papike J. Washington, D.C.: Mineralogical Society of America. pp. 3–1–3–398.

Bridges J. C., Franchi I. A., and Green S. F. 2007. Stardust Microcrater residue compositional groups (abstract #2180). 38th Lunar and Planetary Science Conference. CD-ROM.

Brownlee D., Tsou P., Aléon J., Alexander C. M. O'D., Araki T., Bajt S., Baratta G. A., Bastien R., Bland P., Bleuet P., Borg J., Bradley J. P., Brearley A., Brenker F., Brennan S., Bridges J. C., Browning N. D., Brucato J. R., Bullock E., Burchell M. J., Busemann H., Butterworth A., Chaussidon M., Cheuvront A., Chi M., Cintala M. J., Clark B. C., Clemett S. J., Cody G., Colangeli L., Cooper G., Cordier P., Daghlian C., Dai Z., d'Hendecourt L., Djouadi Z., Dominguez G., Duxbury T., Dworkin J. P., Ebel D. S., Economou T. E., Fakra S., Fairey S. A. J., Fallon S., Ferrini G., Ferroir T., Fleckenstein H., Floss C., Flynn G., Franchi I. A., Fries M., Gainsforth Z., Gallien J.-P., Genge M., Gilles M. K., Gillet P., Gilmour J., Glavin D. P., Gounelle M., Grady M. M., Graham G. A., Grant P. G., Green S. F., Grossemy F., Grossman L., Grossman J. N., Guan Y., Hagiya K., Harvey R., Heck P., Herzog G. F., Hoppe P., Hörz F., Huth J., Hutcheon I. D., Ignatyev K., Ishii H., Ito M., Jacob D., Jacobsen C., Jacobsen S., Jones S., Joswiak D., Jurewicz A., Kearsley A. T., Keller L. P., Khodja H., Kilcoyne A. L. D., Kissel J., Krot A., Langenhorst F., Lanzirotti A., Le L., Leshin L. A., Leitner J., Lemelle L., Leroux H., Liu M.-C., Luening K., Lyon I., MacPherson G., Marcus M. A., Marhas K., Marty B., Matrajt G., McKeegan K., Meibom A., Mennella V., Messenger K., Messenger S., Mikouchi T., Mostefaoui S., Nakamura T., Nakano T., Newville M., Nittler L. R., Ohnishi I., Ohsumi K., Okudaira K., Papanastassiou D. A., Palma R., Palumbo M. E., Pepin R. O., Perkins D., Perronnet M., Pianetta P., Rao W., Rietmeijer F. J. M., Robert F., Rost D., Rotundi A., Ryan R., Sandford S. A., Schwandt C. S., Schlutter D., Sheffield-Parker J., Simionovici A., Simon S., Sitnitsky I., Snead C. J., Spencer M. K., Stadermann F. J., Steele A., Stephan T., Stroud R., Susini J., Sutton S. R., Suzuki Y., Taheri M., Taylor S., Teslich N., Tomeoka K., Tomioka N., Toppani A., Trigo-Rodríguez J. M., Troadec D., Tsuchiyama A., Tuzzolino A. J., Tyliszczak T., Uesugi K., Velbel M., Vellenga J., Vicenzi E., Vincze L., Warren J., Weber I., Weisberg M., Westphal A. J., Wirick S., Wooden D., Wopenka B., Wozniakiewicz P., Wright I., Yabuta H., Yano H., Young E. D., Zare R. N., Zega T., Ziegler K., Zimmermann L., Zinner E., and Zolensky M. 2006. Comet 81P/Wild 2 under a microscope. *Science* 314:1711–1716.

Bunch T. E., Schultz P., Cassen P., Brownlee D., Pdalak M., Lissauer J., Reynolds R., and Chang S. 1991. Are some chondrule rims formed by impact processes? Observations and experiments. *Icarus* 91:76–92.

Burchell M. J. and Kearsley A. T. 2009. Short period Jupiter family comets after stardust. *Planetary and Space Science* 57:1146–1161.

Burchell M. J., Cole M. J., McDonnell J. A. M., and Zarnecki J. C. 1999. Hypervelocity impact studies using the 2 MV Van de Graaff accelerator and two-stage light gas gun of the University of Kent at Canterbury. *Measurement Science Technology* 10:41–50.

Burchell M. J., Creighton J. A., Cole M. J., Mann J., and Kearsley A. T. 2001. Capture of particles in hypervelocity impacts in aerogel. *Meteoritics & Planetary Science* 36:209–221.

Burchell M. J., Graham G., and Kearsley A. 2006a. Cosmic dust collection in aerogel. *Annual Reviews of Earth and Planetary Science* 34:385–418.

Burchell M. J., Mann J., Creighton J. A., Kearsley A. T., Graham G., and Franchi I. A. 2006b. Identification of minerals and meteoritic materials via Raman techniques after capture in hypervelocity impacts on aerogel. *Meteoritics & Planetary Science* 41:217–232.

Burchell M. J., Fairey S. A. J., Wozniakiewicz P., Brownlee D. E., Hörz F., Kearsley A. T., See T. H., Westphal A., Green S. F., and Trigo-Rodríguez J. M. 2008. Characteristics of cometary dust tracks in Stardust aerogel and laboratory calibrations. *Meteoritics & Planetary Science* 43:23–40.

Burchell M. J., Fairey S. A. J., Foster N. J., and Cole M. J. 2009. Hypervelocity capture of particles in aerogel: Dependence on aerogel properties. *Planetary and Space Science* 57:58–70.

Changela H. G. and Bridges J. C. 2009. TEM study of alteration assemblages in the nakhlites: Variation with burial depth on Mars (abstract #2302). 40th Lunar and Planetary Science Conference. CD-ROM.

Choi B.-G. and Wasson J. T. 2003. Microscale oxygen isotopic exchange and formation of magnetite in the Ningqiang

anomalous carbonaceous chondrite. *Geochimica et Cosmochimica Acta* 67:4655–4660.

De Faria D. L. A., Venâncio Silva S., and De Oliveira M. T. 1997. Raman microspectroscopy of some iron oxides and oxyhydroxides. *Journal of Raman Spectroscopy* 28:873–878.

Farnham T. L. and Schleicher D. G. 2005. Physical and compositional studies of comet 81P/Wild 2 at multiple apparitions. *Icarus* 173:533–558.

Flynn G. J. 2008. Physical, chemical, and mineralogical properties of comet 81P/Wild 2 particles collected by Stardust. *Earth Moon and Planets* 102:447–459.

Flynn G. J., Bleuet P., Borg J., Bradley J. P., Brenker F. E., Brennan S., Bridges J., Brownlee D. E., Bullock E. S., Burghammer M., Clark B. C., Dai Z. R., Daghlian C. P., Djouadi Z., Fakra S., Ferroir T., Floss C., Franchi I. A., Gainsforth Z., Gallien J.-P., Gillet P., Grant P. G., Graham G. A., Green S. F., Grossemy F., Heck P. R., Herzog G. F., Hoppe P., Hörz F., Huth J., Ignatyev K., Ishii H. A., Janssens K., Joswiak D., Kearsley A. T., Khodja H., Lanzirotti A., Leitner J., Lemelle L., Leroux H., Luening K., MacPherson G. J., Marhas K. K., Marcus M. A., Matrajt G., Nakamura T., Nakamura-Messenger K., Nakano T., Newville M., Papanastassiou D. A., Pianetta P., Rao W., Riekel C., Rietmeijer F. J. M., Rost D., Schwandt C. S., Sheffield-Parker J., Simionovici A., Sitnitsky I., Snead C. J., Stadermann F. J., Stephan T., Stroud R. M., Susini J., Suzuki Y., Sutton S. R., Taylor S., Teslich N., Troadec D., Tsou P., Tsuchiyama A., Uesugi K., Vekemans B., Vicenzi E. P., Vincze L., Westphal A. J., Wozniakiewicz P., Zinner E., and Zolensky M. E. 2006. Elemental compositions of comet 81P/Wild 2 samples collected by Stardust. *Science* 314:1731–1735.

Grossemy F., Borg J., Djouadi Z., Simionovici A., Lemelle L., Eichert D., Deboffle D., Westphal A. J., and Snead C. 2008. In-situ Fe XANES of extraterrestrial grains trapped in aerogel collectors: An analytical test for the interpretation of Stardust samples analyses. *Planetary and Space Science* 55:966–973.

Haggerty S. E. and Baker I. 1967. The alteration of olivine in basaltic and associated lavas. Part I. High temperature alteration. *Contributions to Mineralogy and Petrology* 16:233–257.

Hörz F., Bastien R., Borg J., Bradley J. P., Bridges J. C., Brownlee D. E., Burchell M. J., Chi M., Cintala M. J., Dai Z. R., Djouadi Z., Dominguez G., Economou T. E., Fairey S. A. J., Floss C., Franchi I. A., Graham G. A., Green S. F., Heck P., Hoppe P., Huth J., Ishii H., Kearsley A. T., Kissel J., Leitner J., Leroux H., Marhas K., Messenger K., Schwandt C. S., Snead C., Stadermann F. J., Stephan T., Stroud R., Teslich N., Trigo-Rodríguez J. M., Tuzzolino A. J., Troadec D., Tsou P., Warren J., Westphal A., Wozniakiewicz P., Wright I., and Zinner E. 2006. Impact features on Stardust: Implications for comet 81P/Wild 2 dust. *Science* 314:1716–1719.

Hörz F., Cintala M. J., See T. H., and Nakamura-Messenger K. 2008. Impact experiments with Al_2O_3 projectiles into aerogel (abstract #1391). 39th Lunar and Planetary Science Conference. CD-ROM.

Ishii H. A., Bradley J. P., Dai Z. R., Chi M. F., Kearsley A. T., Burchell M. J., Browning N. D., and Molster F. 2008. Comparison of comet 81P/Wild 2 dust with interplanetary dust from comets. *Science* 319:447–450.

Joswiak D. J., Brownlee D. E., and Matrajt G. 2008. Surprisingly high abundance of Na and Cr-rich calcic pyroxenes in Stardust tracks (abstract #2177). 39th Lunar and Planetary Science Conference. CD-ROM.

Kearsley A. T., Borg J., Graham G. A., Burchell M. J., Cole M. J., Leroux H., Bridges J. C., Hörz F., Wozniakiewicz P. J., Bland P. A., Bradley J. P., Dai Z. R., Teslich N., Westphal A., See T., Hoppe P., Heck P. R., Huth J., Stadermann F. J., Floss C., Marhas K., Zinner E., Stroud R., Stephan T., and Leitner J. 2008. Dust from comet Wild 2: interpreting particle size, shape, structure and composition from impact features on the Stardust aluminium foils. *Meteoritics & Planetary Science* 43: 41–74.

Keller L. P., Thomas K. L., and McKay D. S. 1992. An Interplanetary dust particle with links to CI chondrites. *Geochimica et Cosmochimica Acta* 56:1409–1412.

Leroux H., Rietmeijer F. J. M., Velbel M. A., Brearley A. J., Jacob D., Langenhorst F., Bridges J. C., Zega T. J., Stroud R. M., Cordier P., Harvey R. P., Lee M., Gounelle M., and Zolensky M. E. 2008. A TEM study of thermally modified comet 81P/Wild 2 dust particles by interaction with the aerogel matrix during the Stardust capture process. *Meteoritics & Planetary Science* 43:97–120.

Madsen M. B., Mørup S., Costa T. V. V., Knudsen J. M., and Olsen M. 1986. Superparamagnetic component in the Orgueil meteorite and Mössbauer spectroscopy studies in applied magnetic fields. *Nature* 321:501–503.

Marcus M. A., Fakra S., Westphal A. J., Snead C. J., Keller L. P., Kearsley A., and Burchell M. J. 2008. Smelting of Fe-bearing glass during hypervelocity capture in aerogel. *Meteoritics & Planetary Science* 43:87–96.

Martin T. P., Merlin R., Huffman D. R., and Cardona M. 1977. Resonant two magnon Raman scattering in α-Fe_2O_3. *Solid State Communications* 22:565–567.

Massey M. J., Baier U., Merlin R., and Weber W. H. 1990. Effects of pressure and isotopic substitution on the Raman spectrum of α-Fe_2O_3: Identification of two-magnon scattering. *Physical Review B* 41:7822–7827.

Morlok A., Bischoff A., Stephan T., Floss C., Zinner E., and Jessberger E. K. 2006. Brecciation and chemical heterogeneities of CI chondrites. *Geochimica et Cosmochimica Acta* 70:5371–5394.

Nakamura T., Noguchi T., Tsuchiyama A., Ushikubo T., Kita N. T., Valley J. W., Zolensky M. E., Kakazu Y., Sakamoto K., Mashio E., Uesugi K., and Nakano T. 2008. Chondrule like objects in short-period comet 81P/Wild 2. *Science* 321:1664–1667.

Noble S. K., Pieters C. M., and Keller L. P. 2007. An experimental approach to understanding the optical effects of space weathering. *Icarus* 192:629–642.

Noguchi T., Nakamura T., Okudaira K., Yano H., Sugita S., and Burchell M. J. 2007. Thermal alteration of hydrated minerals during hypervelocity capture to silica aerogel at the flyby speed of Stardust. *Meteoritics & Planetary Science* 42:357–372.

Pieters C. M., Taylor L. A., Noble S. K., Keller L. P., Hapke B., Morris R. V., Allen C. A., McKay D. S., and Wentworth S. 2000. Space weathering on airless bodies: Resolving a mystery with lunar samples. *Meteoritics & Planetary Science* 35:1101–1107.

Pingitore N. E., Iglesias A., Bruce A., Lytle F., and Wellington G. M. 2002. Valences of iron and copper in coral skeleton:

X-ray absorption spectroscopy analysis. *Microchemical Journal* 71:205–210.

Prietzel J., Thieme J., Eusterhues K., and Eichert D. 2007. Iron speciation in soils and soil aggregates by synchrotron-based X-ray microspectroscopy (XANES, mu-XANES). *European Journal of Soil Science* 58:1027–1041.

Rietmeijer F. J. M. 1998. Interplanetary dust particles. In *Planetary materials*, edited by Papike J. Washington, D.C.: Mineralogical Society of America. pp. 2–1–2–95.

Rietmeijer F. J. M. 2004. First report of taenite in an asteroidal interplanetary dust particle: Flash-heating simulates nebular dust evolution (abstract #1060). 35th Lunar and Planetary Science Conference. CD ROM.

Rietmeijer F. J. M., Nakamura T., Tsuchiyama A., Uesugi K., and Nakano T. 2008. Origin and formation of iron-silicide phases in the aerogel of the Stardust mission. *Meteoritics & Planetary Science* 42:121–134.

Shebanova O. N. and Lazor P. 2003. Raman study of magnetite (Fe_3O_4): Laser induced thermal effects and oxidation. *Jounal of Raman Spectroscopy* 34:845–852.

Trigo-Rodríguez J. M., Domínguez G., Burchell M. J., Hörz F., and Llorca J. 2008. Bulbous tracks arising from hypervelocity capture in aerogel. *Meteoritics & Planetary Science* 43:75–86.

Tsou P., Brownlee D. E., Laurance M. E., Hrubesh L., and Albee A. 1988. Intact capture of hypervelocity micrometeoroid analogs. Proceedings, 19th Lunar and Planetary Science Conference. pp. 1205–1206.

Westphal A. J., Snead C., Borg J., Quirico E., Raynal P. I., Zolensky M. E., Ferrini G., Colangeli L., and Palumbo P. 2002. Small hypervelocity particles captured in aerogel collectors: Location, extraction, handling and storage. *Meteoritics & Planetary Science* 37:855–865.

Westphal A. J., Brownlee D. E., Butterworth A. L., Fakra S., Gainsforth Z., Joswiak D., Marcus M. A., Snead C. J., and Ogliore R. C. 2008. Oxidation state of Fe in the Jupiter-family comet Wild 2 (abstract #2133). 39th Lunar and Planetary Science Conference. CD-ROM.

Zhou B. and He D. 2008. Raman spectrum of vanadium pentoxide from density-functional perturbation theory. *Journal of Raman Spectroscopy* 39:1475–1481.

Zolensky M. E. and Lindstrom D. J. 1992. Mineralogy of 12 large "chondritic" interplanetary dust particles. Proceedings 19th Lunar and Planetary Science Conference 22:161–169.

Zolensky M. E., Zega T. J., Yano H., Wirick S., Westphal A. J., Weisberg M. K., Weber I., Warren J. L., Velbel M. A., Tsuchiyama A., Tsou P., Toppani A., Tomioka N., Tomeoka K., Teslich N., Taheri M., Susini J., Stroud R., Stephan T., Stadermann F. J., Snead C. J., Simon S. B., Simionovici A, Rietmeijer F. J. M., Rao W., Perronnet M. C., Papanastassiou D. A., Okudaira K., Ohsumi K., Ohnishi I., Nakamura-Messenger K., Nakamura T., Mostefaoui S., Mikouchi T., Meibom A., Matrajt G., Marcus M. A., Leroux H., Lemelle L., Le L., Lanzirotti A., Langenhorst F., Krot A. N., Keller L. P., Kearsley A. T., Joswiak D., Jacob D., Ishii H., Harvey R., Hagiya K., Grossman L., Grossman J. N., Graham G. A., Gounelle M., Gillet P., Genge M. J., Flynn G., Ferroir T., Fallon S., Ebel D. S., Dai Z. R., Cordier P., Clark B., Chi M., Butterworth A. L., Brownlee D. E., Bridges J. C., Brennan S., Brearley A., Bradley J. P., Bleuet P., Bland P. A., and Bastien R. 2006. Mineralogy and petrology of comet 81P/Wild 2 nucleus samples. *Science* 314:1735–1739.

Zolensky M. E., Krot A. N., and Benedix G. 2008. Record of low-temperature alteration in asteroids. *Reviews of Mineralogy and Geochemistry* 68:429–462.